

Two-dimensional infrared-Raman spectroscopy as a probe of water's tetrahedrality

Tomislav Begušić^{1, a)} and Geoffrey A. Blake^{1, 2, b)}

¹⁾*Division of Chemistry and Chemical Engineering, California Institute of Technology, Pasadena, California 91125, USA*

²⁾*Division of Geological and Planetary Sciences, California Institute of Technology, Pasadena, California 91125, USA*

(Dated: 1 November 2022)

Two-dimensional spectroscopic techniques combining terahertz (THz), infrared (IR), and visible pulses offer a wealth of information about coupling among vibrational modes in molecular liquids, thus providing a promising probe of their local structure. However, the capabilities of these spectroscopies are still largely unexplored due to experimental limitations and inherently weak nonlinear signals. Here, through a combination of equilibrium-nonequilibrium molecular dynamics (MD) and a tailored spectrum decomposition scheme, we identify a relationship between the tetrahedral order of liquid water and its two-dimensional IR-IR-Raman (IIR) spectrum. The structure-spectrum relationship can explain the temperature dependence of the spectral features corresponding to the anharmonic coupling between low-frequency intermolecular and high-frequency intramolecular vibrational modes of water. In light of these results, we propose new experiments and discuss the implications for the study of tetrahedrality of liquid water.

^{a)}Electronic mail: tbegusic@caltech.edu

^{b)}Electronic mail: gab@caltech.edu

Understanding the dynamical structure of liquid water is paramount to a number of chemical and biological processes. In particular, the tetrahedral ordering of molecules, stemming from the directionality of hydrogen bonds, has been proposed as the origin of water’s anomalous behavior in the liquid phase.¹ However, the tetrahedral structure of water has also been contested both computationally² and experimentally.³ To date, most of our microscopic, structural information about liquid water comes from molecular dynamics (MD) simulations, which depend strongly on the choice of electronic structure theory or force field parametrization. In contrast, experimental tools capable of studying the local arrangement of water molecules remain scarce.⁴ For example, common techniques that probe the structure of liquids, such as X-ray and neutron scattering, typically report on highly time-averaged quantities, and can be accurately reproduced with very different structural motifs.^{2,5–7} Vibrational spectroscopy, such as IR absorption and Raman scattering, offers complementary information about the strength of intermolecular hydrogen bonds, which depends on instantaneous, local arrangement of water molecules.⁸ Different spectral regions have been probed to investigate intermolecular hydrogen-bond bending and stretching modes (up to 300 cm^{-1}), frustrated rotational (librational) modes ($400–1000\text{ cm}^{-1}$), intramolecular bending (1650 cm^{-1}) and stretching ($3000–3800\text{ cm}^{-1}$) modes, as well as combination bands between intermolecular and intramolecular modes. Reported experiments and simulations range from high-resolution spectroscopy on molecular clusters^{9–12} to studies of interfacial^{13–15} or bulk water.^{16–25} Recently, a joint experimental and computational study^{26,27} of the temperature dependence of the Raman spectrum of liquid water revealed a clear structure-spectrum relationship between the local tetrahedral order parameter,²⁸ a measure of structuring of liquid water, and frequency shifts and intensities of spectral peaks. In fact, the temperature dependence of the spectrum was, in this way, fully explained as a change in the thermal distribution of the tetrahedral order parameter. Yet, conventional, steady-state spectroscopy of liquids typically produces broad, unresolved spectral features and misses dynamical information.

Time-resolved and two-dimensional vibrational spectroscopies have emerged in the past years as probes sensitive to the local water coordination. Even here, however, the long-standing tools of two-dimensional infrared spectroscopy,^{4,29,30} which measures the interaction of light with intramolecular, high-frequency modes, provides only an indirect probe of intermolecular dynamics. To target the low-frequency modes directly, a number of hybrid

spectroscopic techniques have been proposed, involving different sequences of THz, IR, and visible pulses, such as the THz-THz-Raman,^{31–34} THz-Raman-THz, Raman-THz-THz,^{35–38} and THz-IR-Raman (also called THz-IR-visible^{39,40} or TIRV). Their development was enabled by the recent advances in the generation of strong THz pulses that are needed to induce a nonlinear light-matter interaction.⁴¹ The THz-THz-Raman and TIRV methods are related to other two-dimensional IR-Raman techniques, namely the two-dimensional IR doubly vibrationally enhanced⁴² and IR-IR-visible sum-frequency generation spectroscopies.⁴³ For example, TIRV experiments have revealed unambiguous spectral signatures of coupling between the intramolecular O-H stretch and intermolecular hydrogen bond bending and stretching modes.³⁹ Theoretical simulations by Ito and Tanimura⁴⁴ predicted such spectral features and assigned them to both mechanical and electrical anharmonic coupling between the said vibrational modes. Similarly, THz-THz-Raman spectroscopy recently revealed signatures of anharmonic coupling between phonons of ionic solid LiNbO₃.⁴⁵ Finally, Raman-THz-THz and THz-Raman-THz spectroscopies have been used to study the inhomogeneity of liquid water and aqueous solutions,^{46,47} as well as the coupling among intermolecular and intramolecular modes in liquid and solid bromoform.^{48,49} Even so, due to a limited availability of efficient THz emitter materials, not all frequencies have been covered by the reported techniques. Specifically, most two-dimensional hybrid THz-Raman spectroscopies of liquid water targeted hydrogen-bond bending and stretching modes, i.e., frequencies up to 400 cm⁻¹, leaving the water librational dynamics largely unexplored.

Here, we aim to provide new insights into the capabilities of two-dimensional hybrid IR-Raman vibrational spectroscopies. To this end, we study the temperature dependence of the two-dimensional IR-IR-Raman (IIR) spectrum, which is given by the double Fourier (or sine) transform of an appropriate third-order, two-time response function. Since the computational model involves all vibrational modes of the system, the response function covers a broad range of frequencies, which, in practice, can be mapped out only through separate experiments. To date, only the TIRV frequency region has been experimentally measured, although its temperature dependence was not studied. Second, following Ref. 26, we then establish a structure-spectrum relationship by separating the spectral contributions from molecules exhibiting low or high tetrahedral coordination. Third, to justify the molecular dynamics (MD) results at low temperature, we analyze whether nuclear quantum effects are discernible in the two-dimensional IIR spectrum.

RESULTS

Theoretical model

We simulated the IIR response function^{33,44}

$$R(t_1, t_2) = -\frac{1}{\hbar^2} \text{Tr}\{[[\hat{\Pi}(t_1 + t_2), \hat{\mu}(t_1)], \hat{\mu}(0)]\hat{\rho}\} \quad (1)$$

using the equilibrium-nonequilibrium MD approach, in which the quantum-mechanical trace is replaced by a classical average^{50–53}

$$R^{\text{MD}}(t_1, t_2) = \frac{\beta}{\varepsilon} \langle [\Pi(q_{+,t_2}) - \Pi(q_{-,t_2})] \dot{\mu}(q_{-t_1}) \rangle, \quad (2)$$

where $\hat{\rho}$ is the thermal density operator, $\hat{\mu} = \mu(\hat{q})$ is the dipole moment operator, and $\hat{\Pi} = \Pi(\hat{q})$ is the polarizability. q_t denotes the position of a classical trajectory initiated at (q_0, p_0) , whereas $q_{\pm,t}$ corresponds to the initial conditions $(q_{\pm,0} = q_0, p_{\pm,0} = p_0 \pm \varepsilon \mu'(q_0)/2)$ after an instantaneous interaction with the electric field. ε is a free parameter in the calculations and corresponds to the magnitude of the external electric field integrated over the short interaction time. The two-dimensional spectra are computed through a double sine transform^{35,44}

$$R(\omega_1, \omega_2) = \int_0^\infty \int_0^\infty R(t_1, t_2) \sin(\omega_1 t_1) \sin(\omega_2 t_2) dt_1 dt_2. \quad (3)$$

To model water, we used a fast and accurate qTIP4P/F force field,⁵⁵ which has been well studied for spectroscopic simulations.²⁵ To allow for nonlinear dependence of the dipole moments and polarizabilities on nuclear coordinates, we employed the truncated dipole-induced-dipole (DID) model. Following Hamm,³⁷ each water molecule was amended with a permanent anisotropic polarizability, which was used for the evaluation of the induced contributions to the dipoles and polarizabilities. In contrast to the rigid water simulations of Ref. 37, here the permanent polarizability was an explicit function of intramolecular degrees of freedom, according to Ref. 56. We note that more advanced models for the potential energy, dipoles, and polarizabilities of liquid water exist and have been used in the simulation of one- and two-dimensional spectroscopies.^{19,22,24,26,37,57} Nevertheless, our approach is sufficiently accurate for the analysis that is presented in this work. In Fig. 1, we show that it can reproduce the main features of the experimental IR absorption and anisotropic Raman spectra of liquid water. Additional details about the model and MD simulations can be found in the Methods section.

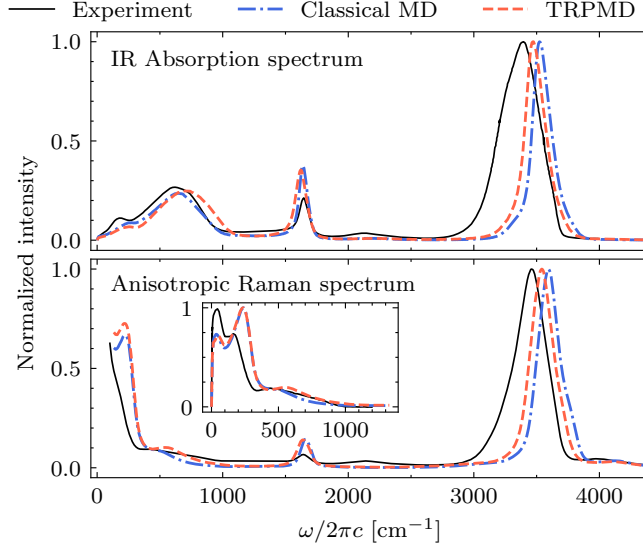


FIG. 1. **Steady-state spectra of water.** IR absorption (top) and anisotropic Raman (bottom) spectra of liquid water at 300 K simulated with the classical MD and TRPMD, compared with the experiments of Refs. 16,27,54. The inset in the bottom panel compares the low-frequency part of the simulated and experimental anisotropic Raman spectra.

Most of the results presented below rely on the validity of the classical MD approach, which neglects quantum-mechanical properties of atomic nuclei. However, due to the presence of light hydrogen atoms, their effect might not be negligible.⁵⁵ Although such nuclear quantum effects on one-dimensional IR and Raman spectra have been well studied using approximate but reliable classical-like methods, no tools similar to the equilibrium-nonequilibrium MD have been available to study nuclear quantum effects on the two-dimensional IR-Raman spectra.^{58–60} Recently, we have developed a new RPMD approach,⁶¹ which reproduces correctly the quantum-mechanical thermal distribution and preserves it during approximate classical dynamics. In this way, the equilibrium-nonequilibrium RPMD method can simulate, at least approximately, the nuclear quantum effects on the two-dimensional IIR spectra. Briefly, the RPMD method⁶² replaces the original quantum-mechanical problem by an extended classical system consisting of N replicas (beads) of the original system connected by harmonic springs. In the limit of $N \rightarrow \infty$, the extended classical system reproduces exact quantum-mechanical thermal distribution, while if $N = 1$, RPMD reduces to classical MD. In our simulations, we used $N = 32$, which is sufficiently large for liquid water in the studied temperature range.²⁵ Since RPMD is known to suffer

from the spurious resonance issue, where unphysical peaks due to artificial harmonic springs appear in the spectra, we employed its thermostatted version (TRPMD).^{63,64} IR absorption and anisotropic Raman spectra simulated with TRPMD are presented in Fig. 1.

Two-dimensional IIR spectrum of liquid water

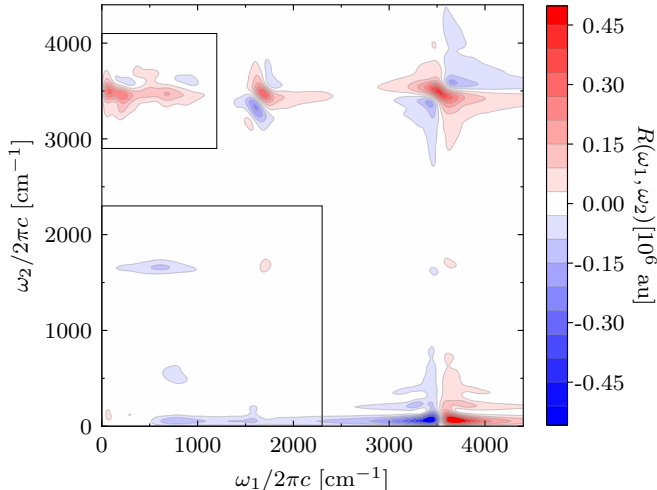


FIG. 2. **Two-dimensional IIR spectrum of liquid water.** IIR spectrum simulated with classical MD at 300 K. Black squares indicate the regions of the spectrum that we studied in more detail, namely the region of terahertz-infrared-visible (TIRV) spectroscopy and the low-frequency region that covers intermolecular modes and the intramolecular bending mode.

Fig. 2 shows the full two-dimensional IIR spectrum of liquid water simulated at 300 K. Apart from the spectral features along the $\omega_1 = \omega_2$ diagonal, which appear due to mechanical or electrical anharmonicity of individual vibrational modes, the spectrum contains off-diagonal peaks that correspond to coupling among different vibrations. Overall, the spectrum qualitatively agrees with the simulation of Ref. 44, with the main difference in the relative intensities of different spectral regions, which can depend strongly on the details of the potential energy, dipole, and polarizability surfaces. In the following, we focus on the two frequency regions indicated by the black rectangles. One region targets the coupling between intermolecular modes ($0 \text{ cm}^{-1} < \omega_1 < 1200 \text{ cm}^{-1}$) and the intramolecular O-H stretch mode ($2900 \text{ cm}^{-1} < \omega_2 < 4100 \text{ cm}^{-1}$), whereas the other covers all low-frequency, intermolecular modes and the intramolecular bend mode. Model simulations of Ref. 44 (see

also Supplementary Section IV) imply that the complex spectral lineshape of the former, which we will refer to as the TIRV region, are a product of interplay between mechanical and electrical anharmonicity. Namely, the mechanical anharmonicity leads to a shape comprising a positive and a negative lobe above and below the central ω_2 frequency, whereas the electrical anharmonicity produces an approximately symmetric feature. In the low-frequency region of interest, we observe a strong peak at about $(600 \text{ cm}^{-1}, 1650 \text{ cm}^{-1})$ due to anharmonic coupling between librations ($400 - 1000 \text{ cm}^{-1}$) and intramolecular bending mode.⁶⁵ The same coupling mechanism is responsible for the combination transition at around 2150 cm^{-1} , also known as the “association” band,^{9,20} in the one-dimensional spectra. Interestingly, this combination band is not captured in our model (see Fig. 1), even though the corresponding two-dimensional spectral feature clearly appears in the IIR spectrum.

Temperature dependence of the IIR spectrum

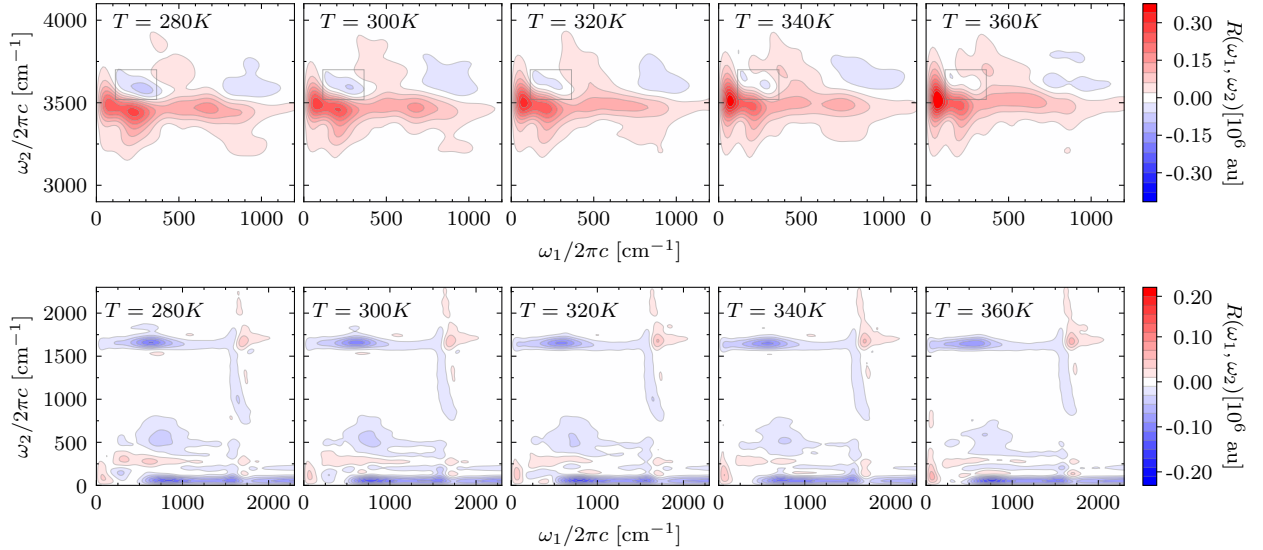


FIG. 3. **Temperature dependence of the IIR spectrum.** Two-dimensional IIR spectra of liquid water simulated with classical MD at different temperatures. Top: TIRV part of the spectrum. The grey squares highlight the peak around $(250 \text{ cm}^{-1}, 3600 \text{ cm}^{-1})$. Bottom: Low-frequency part of the spectrum.

We now turn to the temperature dependence of the two IIR spectral regions (Fig. 3). The TIRV part of the spectrum experiences several changes as the temperature is increased from

280 K to 360 K. At higher temperatures the peaks are blue-shifted along ω_2 , which agrees with the observed trends in the experimental Raman spectra and simulated vibrational density of states.²⁶ In addition, the shape of the spectral peaks changes drastically. The most prominent change in the spectrum is the disappearance of the negative peak around (250 cm^{-1} , 3600 cm^{-1}). According to the interpretation based on model simulations, this indicates that the electrical anharmonicity contribution to the spectrum, marked by strong symmetric lineshape, increases compared to that of the mechanical anharmonicity. Unlike the frequency shift, this feature cannot be accessed through steady-state spectroscopy. Finally, we note that a peak around (400 cm^{-1} , 3700 cm^{-1}) appears at elevated temperature, while the other peak at about (700 cm^{-1} , 3400 cm^{-1}) almost disappears. Interestingly, both of these coupling terms have been discussed as possible origins of the libration-stretch combination band appearing in the anisotropic Raman spectrum of liquid water at 4100 cm^{-1} .^{26,66} The same combination band has also been shown to play an important role in second-order vibrational sum-frequency spectroscopy of interfacial water.¹⁵

The low-frequency region also exhibits strong temperature dependence. For example, the results (see also difference spectra in the Supplementary Fig. 5) clearly indicate a red shift of the libration-bend peak along ω_1 with increasing temperature. This is a straightforward consequence of the equivalent frequency shift found in the linear IR absorption spectrum (see Supplementary Fig. 6), which also agrees with the experimentally observed trend.¹⁷ Furthermore, the two-dimensional IIR spectrum at 280 K contains peaks close to diagonal, around $\omega_1 = \omega_2 = 250 \text{ cm}^{-1}$, due to mechanical anharmonicity of the hydrogen-bond stretching modes. These seem to progressively disappear at elevated temperatures. Importantly, this change in intensity could not be simply predicted from the one-dimensional spectra, which show little change in the intensity of the 250 cm^{-1} band. We note, however, that the features in this congested spectral region could be affected by the short times available from our simulations and by artificial broadening. Longer simulations are possible with rigid water models, which have been used to study explicitly the intermolecular modes and corresponding two-dimensional THz-Raman signals in the time domain.^{37,51}

Spectral signatures of water’s tetrahedrality in the IIR spectrum

To understand the temperature-dependent spectral features, we follow the work of Morawietz et al.,²⁶ where the temperature effects were analyzed in relation to the local structuring around individual water molecules. This can be quantified by the local tetrahedral order parameter Q ,^{67–69} which measures how the arrangement of the four neighboring water molecules deviates from the ideal tetrahedral arrangement around the central one. By convention, $Q = 1$ for a perfect tetrahedral arrangement, while $Q = 0$ for an ideal gas. The distribution of Q at thermal equilibrium exhibits a strong temperature dependence and a clear isosbestic point at $Q \approx 0.67$ (see Fig. 4a), attributed to the existence of two components whose populations change with temperature.²⁶

To directly correlate the local tetrahedral order parameter with the spectral features observed in the two-dimensional IIR spectra, we decomposed the spectrum into contributions of individual molecules (see Supplementary Section VII). Then, we simulated the spectra (see Fig. 4b) originating predominantly from the molecules with either high ($Q > 0.72$) or low ($Q < 0.62$) local tetrahedral order parameter. The two IIR spectra align remarkably well with the observed temperature-dependent changes. Specifically, the high-order TIRV spectrum (Fig. 4b, top right) exhibits a clear mechanical anharmonic coupling feature with a positive and a negative lobe at $\omega_1 \approx 250 \text{ cm}^{-1}$, whereas the corresponding low-order spectrum contains a strong symmetric peak, indicating electrical anharmonic coupling between the hydrogen-bond modes and O-H stretch. In addition, the libration-stretch peak at (400 cm^{-1} , 3700 cm^{-1}) appears almost exclusively in molecules with a low tetrahedral order. Similarly, the libration-bend peak in the low-frequency part the spectrum (bottom panels of Fig. 4b) appears at lower ω_1 frequencies for low Q . Overall, the temperature dependence of the IIR spectra can be almost exclusively assigned to the changes in the distribution of the local tetrahedral order parameter and the effect of the local structure on the spectral features. Therefore, TIRV spectroscopy expanded into the water libration frequency range, i.e., with ω_1 covering up to $\approx 800 \text{ cm}^{-1}$ could provide an alternative probe of the local molecular structure in liquid water and aqueous solutions. Importantly, the spectral changes in IIR are more drastic, and therefore more sensitive to local ordering, than the frequency shifts observed in conventional, one-dimensional IR and Raman spectroscopies.

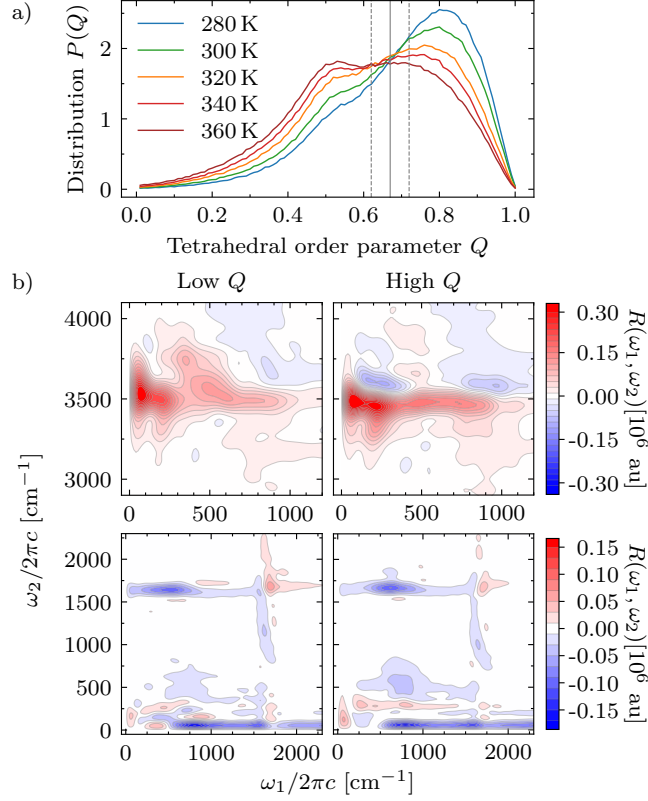


FIG. 4. **Effect of tetrahedral order on the IIR spectra.** Top: Distribution of the local tetrahedral order parameter of liquid water as a function of temperature. The isosbestic value is indicated by the solid, grey line. Two dashed, grey lines specify the region excluded from subsequent two-dimensional IIR spectra simulations ($0.62 < Q < 0.72$). Bottom panels: Two-dimensional IIR spectra of water molecules with high ($Q > 0.72$, top) or low ($Q < 0.62$, bottom) tetrahedral order parameter, simulated with the classical equilibrium-nonequilibrium MD approach at 320 K.

Nuclear quantum effects on the two-dimensional IIR spectrum

Finally, we report the first TRPMD simulation of the two-dimensional IIR spectrum of liquid water and compare it with the MD simulation in Fig. 5. Some nuclear quantum effects can be easily explained in terms of the differences between one-dimensional spectra (see Supplementary Fig. 7). Namely, the red-shifted O-H stretch band in the TRPMD steady-state spectra reflects in a red shift along ω_2 of the spectral features in the TIRV spectrum (Fig. 5, top). Furthermore, the libration-stretch peak shifts from $\omega_1 \approx 700 \text{ cm}^{-1}$ in the MD spectrum to $\omega_1 \approx 800 \text{ cm}^{-1}$ in TRPMD, which aligns with the differences between MD and TRPMD IR absorption spectra. In the low-frequency part of the spectrum, the

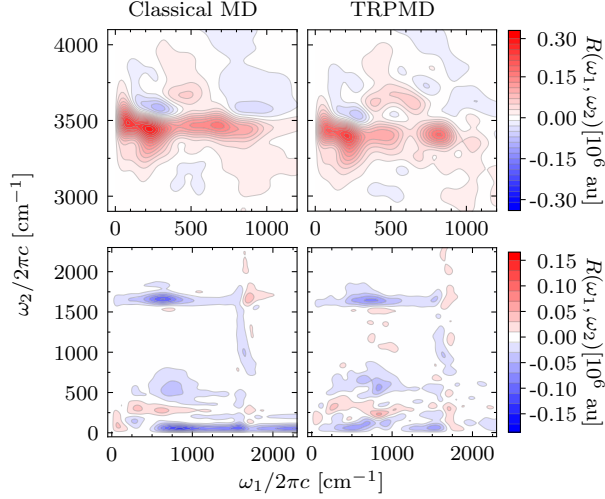


FIG. 5. **Nuclear quantum effects on the IIR spectrum.** Two-dimensional IIR spectra of liquid water at 280 K, simulated with equilibrium-nonequilibrium MD (top) and TRPMD .

libration-bend peak is analogously shifted along ω_1 . However, some features cannot be understood from comparison with the one-dimensional spectra, such as the absence of the strong negative feature at $(\omega_1 \approx 750 \text{ cm}^{-1}, \omega_2 \approx 50 \text{ cm}^{-1})$ in TRPMD or the change in the spectral lineshapes in the TIRV region at $\omega_1 > 400 \text{ cm}^{-1}$. Nevertheless, these differences are not sufficiently large to alter the above conclusions based on classical MD simulations.

DISCUSSION

To conclude, we have presented MD and TRPMD simulations of the two-dimensional IIR spectra of liquid water. By analyzing the temperature dependence of the spectrum, we have identified features that report on the degree of local tetrahedral ordering in the first coordination shell. We envision that this structure-spectrum relationship could also be used to probe the structure of complex aqueous systems, such as confined water and aqueous solutions. Further computational work is needed to confirm that IIR spectra of such systems can be broadly mapped to the local tetrahedral order parameter. Our work demonstrates that the temperature dependence of such two-dimensional spectra can be used in combination with computational modeling to gain insight into the structure of complex liquids.

Furthermore, the simulations presented here imply that the contributions of mechanical

and electrical anharmonic coupling change as a function of local tetrahedrality, which cannot be studied with conventional, one-dimensional spectroscopy. Specifically, the electrical anharmonicity dominates at higher temperatures, where the tetrahedral order parameter is low, whereas the mechanical coupling, due to the anharmonic terms in the potential energy surface, are pronounced at lower temperature and higher tetrahedrality. The spectral region in which we identified the main signature of tetrahedrality has been studied experimentally.³⁹ However, the experiments could only measure an absolute value Fourier transform spectrum (see Supplementary Section III and Supplementary Fig. 3), which is quite different from the real sine transform discussed here and in Ref. 44. Hence, further experimental work is needed to successfully measure the features that, according to our prediction, correlate with the local tetrahedral order parameter.

Finally, we observe that the $400 \text{ cm}^{-1} < \omega_1 < 1000 \text{ cm}^{-1}$ region of the IIR spectrum, corresponding to the librations of water molecules, carries rich information about liquid water and should be further explored experimentally. In particular, such studies could provide additional information on the combination bands appearing in IR absorption and Raman scattering spectra that have challenged physical chemists for decades.

METHODS

Dipole moment and polarizability models

The induced dipole moments and polarizabilities were modeled as³⁷

$$\vec{\mu}^{\text{ind}} = \sum_{\substack{i,j \\ i \neq j}} \mathbf{\Pi}_i \cdot \vec{E}_{ij}, \quad (4)$$

$$\mathbf{\Pi}^{\text{ind}} = - \sum_{\substack{i,j \\ i \neq j}} \mathbf{\Pi}_i \cdot \mathbf{T}_{ij} \cdot \mathbf{\Pi}_j, \quad (5)$$

where $\vec{E}_{ij} = \sum_{a \in \{\text{O}, \text{H1}, \text{H2}\}} Q_{ja} \vec{r}_{ja,i\text{O}} / r_{ja,i\text{O}}^3$ is the electric field produced by molecule j on the oxygen atom of molecule i , $\mathbf{T}_{ij} = \mathbf{T}(\vec{r}_{j\text{O},i\text{O}})$, $\mathbf{T}(\vec{r}) = (r^2 - 3\vec{r} \otimes \vec{r})/r^5$ is the dipole-dipole interaction tensor, $\vec{r}_{ja,i\text{O}} = \vec{r}_{ja} - \vec{r}_{i\text{O}}$, \vec{r}_{ja} denotes the position vector of atom $a \in \{\text{O}, \text{H1}, \text{H2}\}$ of molecule j , Q_{ja} is its partial qTIP4P/F charge, $r = \|\vec{r}\|$ denotes the norm of vector \vec{r} , and \otimes is the outer product of two vectors. Permanent dipole moment of molecule i was $\vec{\mu}_i = \sum_{a \in \{\text{O}, \text{H1}, \text{H2}\}} Q_{ia} \vec{r}_{ia} / c$, where $c = 1.3$ is a scaling factor that reduces the dipole

moment of water to its gas-phase value.^{37,52} The permanent polarizability of each molecule i , $\mathbf{\Pi}_i \equiv \mathbf{\Pi}_i(\vec{r}_{iO}, \vec{r}_{iH1}, \vec{r}_{iH2})$, was computed according to Ref. 56 in the molecular reference frame and rotated into the laboratory frame. Then, the total dipole moment and polarizability are given by

$$\vec{\mu} = \sum_i \vec{\mu}_i + \vec{\mu}^{\text{ind}}, \quad (6)$$

$$\mathbf{\Pi} = \sum_i \mathbf{\Pi}_i + \mathbf{\Pi}^{\text{ind}}. \quad (7)$$

Finally, we note that the sums over i in all expressions above are taken over the molecules in a unit cell, while the sums over j extend to infinity beyond the central unit cell. Due to the slow convergence of Coulomb interactions in the direct space, we used Ewald summation for the electric field \vec{E}_{ij} and tensor \mathbf{T}_{ij} .^{22,52}

Computational details

Classical thermal average of equation (2) of the main text was evaluated by sampling from 5 independent NVT trajectories, each equilibrated for 100 ps, of a water box with 64 molecules and the cell parameter adjusted to the experimental density at any given temperature. Initial structure was taken from Ref. 24. A time step of $\Delta t = 0.25$ fs, second order symplectic integrator, and a Langevin thermostat with the time constant $\tau = 100$ fs were used throughout. From 2560 initial samples collected in this way, we launched 25 ps NVE equilibrium trajectories, along which we collected the dipole moments and polarizabilities every 4 steps (1 fs) and the derivatives of the dipole moment every 1000 steps (250 fs). Finally, starting from positions at which the dipole derivatives were evaluated, “nonequilibrium” trajectories, i.e., with modified initial momenta $p_{\pm,0}$ (see main text), were propagated for 1000 steps (250 fs). This generated 2.56×10^5 samples for equation (2) of the main text, which is comparable to the numbers used in Refs. 39,51,52, and the response function was computed for 250 fs in both t_1 and t_2 . The statistical error was estimated using bootstrapping and is shown in Supplementary Fig. 1. We set $\varepsilon = 2$, which converts into the electric field magnitude of $E_0 = \varepsilon/\Delta t \approx 10$ V/Å. Weaker electric field was also tested ($\varepsilon = 0.2$ a.u., see Supplementary Fig. 2) in a simulation with the doubled number of initial conditions.

RPMD simulations were performed in a similar way, using 4 independent thermostatted path-integral MD (PIMD) trajectories to produce 512 samples from which TRPMD trajec-

ries were launched. Each TRPMD equilibrium trajectory was propagated for 50 ps (200000 steps) and nonequilibrium trajectories were launched every 1000 steps. In total, this resulted in 1.024×10^5 initial conditions. PIMD trajectories used a path-integral Langevin equation (PILE) thermostat for the normal modes with the centroid coupled to a global velocity rescaling thermostat with $\tau = 100$ fs,⁷⁰ whereas the TRPMD trajectories used a generalized Langevin equation (GLE) thermostat coupled to the normal mode representation of the ring polymer.⁶⁴

Linear absorption and anisotropic Raman spectra were computed from the equilibrium trajectories according to:

$$I^{\text{IR}}(\omega) \propto -\omega \text{Im} \int_0^\infty \langle \vec{\mu}(t) \cdot \dot{\vec{\mu}}(0) \rangle e^{-t^2/2\sigma_t^2} e^{-i\omega t} dt, \quad (8)$$

$$I^{\text{Raman}}(\omega) \propto -A(\omega) \text{Im} \int_0^\infty \langle \text{Tr}[\boldsymbol{\beta}(t) \cdot \dot{\boldsymbol{\beta}}(0)] \rangle e^{-t^2/2\sigma_t^2} e^{-i\omega t} dt, \quad (9)$$

where $\vec{\mu}$ is the dipole moment vector of the cell, $\boldsymbol{\beta}(t) = \boldsymbol{\Pi}(t) - \mathbf{I} \text{Tr}[\boldsymbol{\Pi}(t)]/3$, $\boldsymbol{\Pi}(t)$ is the polarizability tensor, I is the 3×3 identity matrix, and $\sigma_t = 1000$ fs. $A(\omega)$ was different for the two Raman experiments shown in Fig. 1. For the broad-range Raman spectrum shown in the bottom panel of Fig. 1, $A(\omega) = [1 - \exp(-\beta\hbar\omega)]^{-1}$,²⁷ while for the low-frequency part shown in the inset of that figure, which was experimentally measured by optical Kerr effect,¹⁶ $A(\omega) = 1$.

Two-dimensional IIR spectra were computed from the response function according to equation (3) of the main text, but with a damping $f(t_1, t_2) = \exp(-(t_1 + t_2)^{12}/\tau_{12})$, $\tau_{12} = 5 \times 10^{28}$ fs¹², applied prior to taking the discrete sine transform. We used the z -component of the dipole moment and zz -component of the polarizability, resulting in the $zzzz$ -component of the response function. The time-dependent response function is computed in the atomic units of $[\text{length}]^3 \times [\text{dipole}]^2 / ([\text{energy}] \times [\text{time}])^2$ and the corresponding spectra in the atomic units of $[\text{length}]^3 \times [\text{dipole}]^2 / [\text{energy}]^2 \equiv e^2 a_0^5 / E_h^2$.

DATA AVAILABILITY

The data that support the findings of this study, together with the input files and scripts for plotting the data, are openly available in Zenodo repository with the digital object identifier (DOI): 10.5281/zenodo.7265859.

CODE AVAILABILITY

Modified i-PI code used to run MD and TRPMD simulations is available at <https://github.com/tbegusic/i-pi.git>; **encorr** code used for processing the outputs is available at <https://github.com/tbegusic/encorr.git>.

ACKNOWLEDGMENTS

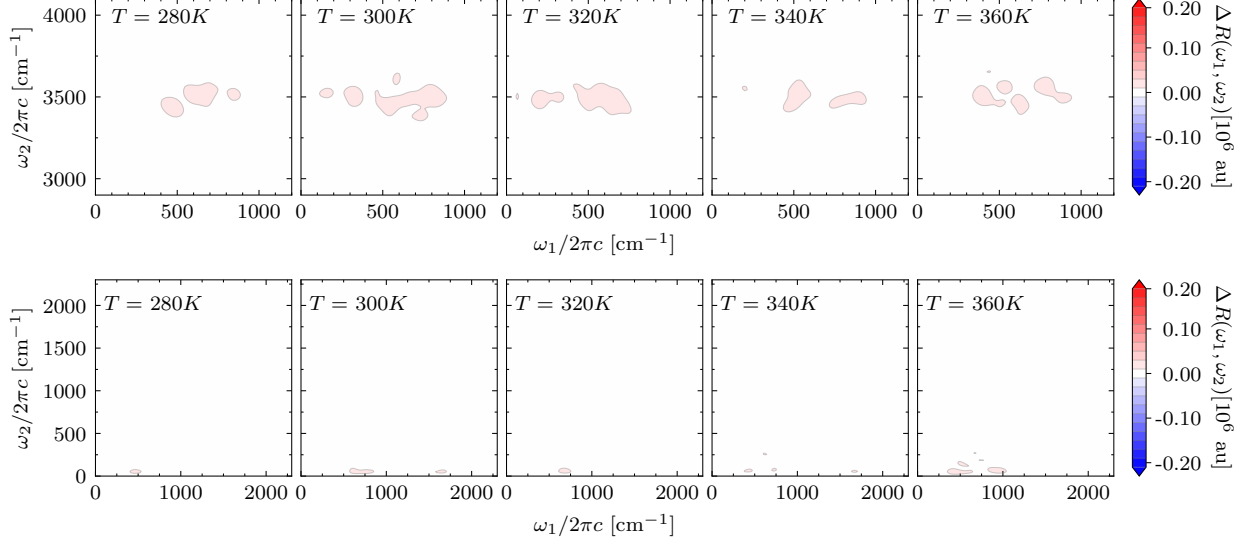
The authors thank Haw-Wei Lin, Roman Korol, and Vignesh C. Bhethanabotla for helpful discussions. T.B. acknowledges financial support from the Swiss National Science Foundation through the Early Postdoc Mobility Fellowship (grant number P2ELP2-199757). The authors gratefully acknowledge support from the National Science Foundation Chemical Structure, Dynamics and Mechanisms program (grant CHE-1665467). The computations presented here were conducted in the Resnick High Performance Computing Center, a facility supported by Resnick Sustainability Institute at the California Institute of Technology.

AUTHOR CONTRIBUTIONS

T.B. conceived the study, implemented the theoretical models and methods, performed the simulations, and analyzed the data; T.B. and G.A.B. discussed the results and wrote the manuscript.

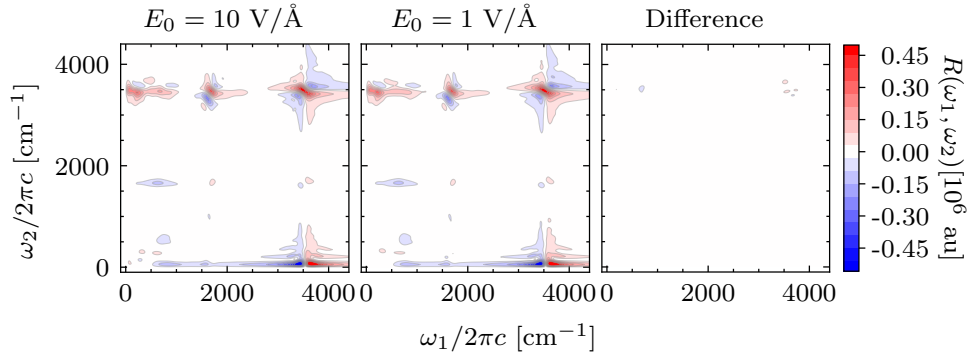
Supplementary information for: Two-dimensional infrared-Raman spectroscopy as a probe of water's tetrahedrality

I. STATISTICAL ERROR



Supplementary Fig. 1. Statistical error of the IIR spectra computed with MD at different temperatures.

II. ELECTRIC FIELD PARAMETER



Supplementary Fig. 2. Difference (right) between IIR spectra simulated using MD at 280 K with $\varepsilon = 2$ ($E_0 = 10$ V/Å, left) and $\varepsilon = 0.2$ ($E_0 = 1$ V/Å, center). The difference is comparable to the statistical error presented in Supplementary Fig. 1.

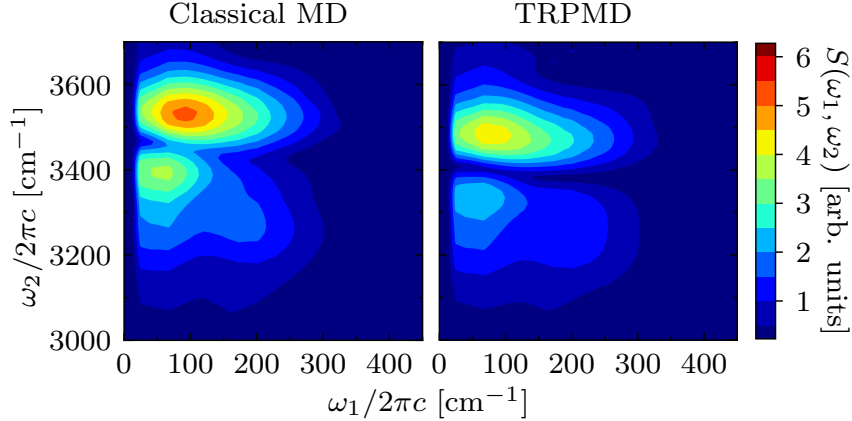
III. COMPARISON WITH THE TIRV EXPERIMENT

To compare with the TIRV experiment and simulations of Ref. 39, we also evaluated

$$\tilde{S}(\omega_1, \omega_2) = |S(\omega_1, \omega_2)E_{\text{THz}}(\omega_1)E_{\text{IR}}(\omega_2 - \omega_1) + S(\omega_1, -\omega_2)E_{\text{THz}}(\omega_1)E_{\text{IR}}(\omega_2 + \omega_1)|, \quad (1)$$

$$S(\omega_1, \omega_2) = \int_0^\infty \int_0^\infty R(t_1, t_2) f(t_1, t_2) e^{-i\omega_1 t_1} e^{-i\omega_2 t_2} dt_1 dt_2, \quad (2)$$

where $E_{\text{THz}}(\omega)$ and $E_{\text{IR}}(\omega)$ are the electric fields obtained as square roots of the intensity spectra presented in Fig. 2b,c of Ref. 39, and $f(t_1, t_2)$ is a damping function defined in the main text (see Methods). $\tilde{S}(\omega_1, \omega_2)$ spectra shown in Fig. 3 exhibit the same nodal structure as the experiment and simulation of Grechko et al. (see Fig. 3 of Ref. 39). The main differences arise due to the limitations of our model, namely the narrow and blue-shifted OH stretch (as shown in Fig. 1 of the main text). In addition, it is difficult to quantify the fraction of resonant signal in the experimental spectrum, as it is mixed with the non-resonant signal that appears in the OH stretch region even in the pure D₂O. In our simulations, D₂O would produce zero signal in this part of the spectrum.



Supplementary Fig. 3. $\tilde{S}(\omega_1, \omega_2)$ of equation (3) evaluated from MD and TRPMD simulations at 300 K.

IV. TWO-DIMENSIONAL MODEL SYSTEM

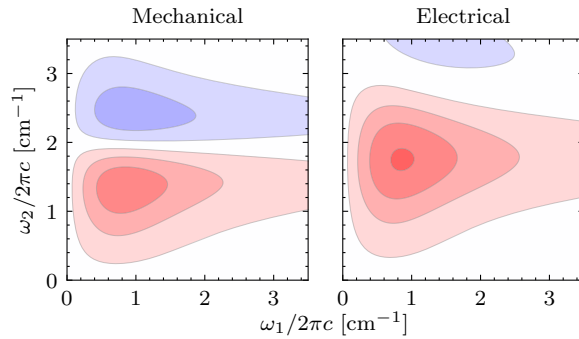
Following Ito and Tanimura,⁴⁴ we simulated the spectra of two different two-dimensional models with harmonic Hamiltonian

$$H_0(q_1, q_2, p_1, p_2) = \sum_{i=1}^2 \frac{p_i^2}{2} + \frac{1}{2} \omega_i^2 q_i^2, \quad (3)$$

$\omega_1 = 0.5$, $\omega_2 = 2$, and $\mu_1 = q_1$ and $\mu_2 = q_2$, where μ_1 and μ_2 are the dipole moments for the interaction with the first and second light pulses. For the model with mechanical anharmonicity, we set the Hamiltonian to

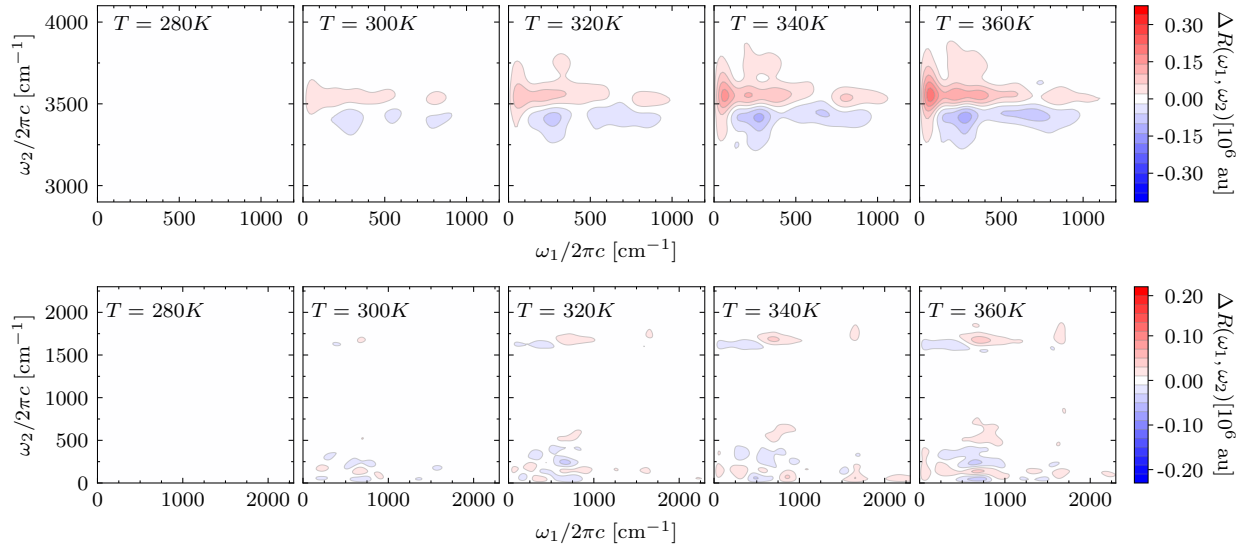
$$H(q_1, q_2, p_1, p_2) = H_0(q_1, q_2, p_1, p_2) + \sum_{i=1}^2 \alpha_i q_i^4 + \lambda q_1 q_2^2, \quad (4)$$

where $\alpha_i = 2.5 \times 10^{-5} \omega_i^4$ and $\lambda = 0.1$, and we set $\Pi = q_2$. The weak quartic terms are added to ensure that the potential is bound. For the model with electrical anharmonicity, the Hamiltonian was quadratic, $H = H_0$, while $\Pi = -0.05 q_1 q_2$. The spectra were simulated with exact quantum mechanics on a grid in position representation, similar to the benchmark simulations of Ref. 61. The response function was simulated for maximum t_1 and t_2 times of 50 with a time step of 0.25. Exponential damping $\exp(-(t_1 + t_2)/\tau)$ with $\tau = 1$ was applied to the response function before evaluating the discrete sine transform.



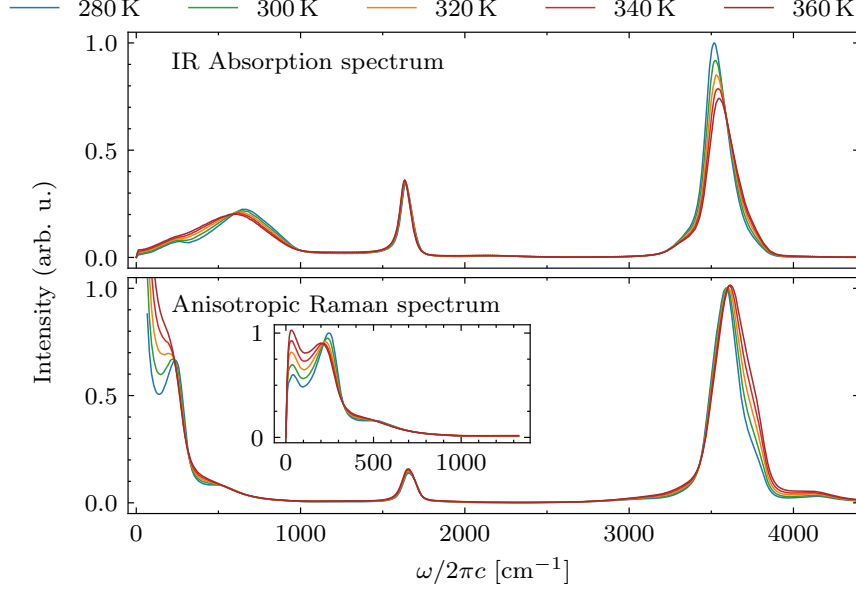
Supplementary Fig. 4. IIR spectra of the two-dimensional model systems with mechanical (left) and electrical (right) anharmonic coupling.

V. DIFFERENCE IIR SPECTRA



Supplementary Fig. 5. Difference between IIR spectra at different temperatures from the spectrum at 280 K. Top: TIRV part of the spectrum. Bottom: Low-frequency part of the spectrum.

VI. TEMPERATURE DEPENDENCE OF IR ABSORPTION AND ANISOTROPIC RAMAN SPECTRA



Supplementary Fig. 6. IR absorption and anisotropic Raman spectra computed using classical MD at different temperatures.

VII. SPECTRUM DECOMPOSITION

Assuming sufficiently small ε , we can expand

$$\Pi(q_{\pm,t}) = \Pi(q_t) \pm \frac{\varepsilon}{2} \frac{d\Pi(q_t)}{dp_0} \cdot \frac{d\mu(q_0)}{dq_0} \quad (5)$$

$$= \Pi(q_t) \pm \frac{\varepsilon}{2} \sum_{i=1}^{N_{\text{mol}}} \frac{d\Pi(q_t)}{dp_{i,0}} \cdot \frac{d\mu(q_0)}{dq_{i,0}} \quad (6)$$

to first order in ε , where the sum goes over N_{mol} molecules, and q_i and p_i denote positions and momenta of atoms in molecule i . Then, it can be shown that

$$R^{\text{MD}}(t_1, t_2) = \sum_{i=1}^{N_{\text{mol}}} R_i^{\text{MD}}(t_1, t_2), \quad (7)$$

where

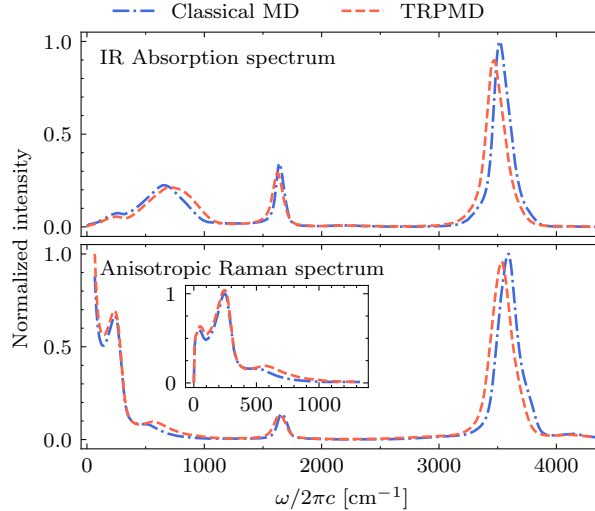
$$R_i^{\text{MD}}(t_1, t_2) = \frac{\beta}{\varepsilon} \langle [\Pi(q_{+,t_2}^{(i)}) - \Pi(q_{-,t_2}^{(i)})] \dot{\mu}(q_{-t_1}) \rangle \quad (8)$$

and $q_{\pm,t}^{(i)}$ is the position vector (all $3N_{\text{atom}}$ coordinates) of a trajectory with initial momentum

$$p_{\pm,0}^{(i)} = p_0 \pm \frac{\varepsilon}{2} \frac{d\mu(q_0)}{dq_{i,0}}, \quad (9)$$

i.e., a trajectory with the electric field applied only on molecule i . In our simulations, we did not decompose the spectrum into individual molecules, but into two groups of molecules exhibiting low and high tetrahedral order parameter, which was computed at time zero. Spectra evaluated in this way were divided by the fractions of molecules of a given order in the thermal distribution, which were $x(Q < 0.62) = \int_0^{0.62} P(Q)dQ = 0.388$ and $x(Q > 0.72) = \int_{0.72}^1 P(Q)dQ = 0.403$ at 320 K. This temperature was chosen for the spectrum decomposition because it contains approximately equal number of molecules in the two groups. Tetrahedral order parameter was evaluated using the `order` code, which was obtained from <https://github.com/ipudu/order.git>.⁶⁹

VIII. MD AND TRPMD IR ABSORPTION AND RAMAN SPECTRA AT 280 K



Supplementary Fig. 7. IR absorption (top) and anisotropic Raman spectra (bottom) simulated with MD and TRPMD at 280 K, analogous to Fig. 1 of the manuscript. All spectra were scaled to the maximum intensity of the MD simulated spectrum.

REFERENCES

- ¹J. Russo, K. Akahane, and H. Tanaka, “Water-like anomalies as a function of tetrahedrality,” *Proc. Nat. Acad. Sci. USA* **115**, E3333–E3341 (2018).
- ²S. Naserifar and W. A. Goddard, “Liquid water is a dynamic polydisperse branched polymer,” *Proc. Nat. Acad. Sci. USA* **116**, 1998–2003 (2019).
- ³P. Wernet, D. Nordlund, U. Bergmann, M. Cavalleri, M. Odelius, H. Ogasawara, L. . Näslund, T. K. Hirsch, L. Ojamäe, P. Glatzel, L. G. M. Pettersson, and A. Nilsson, “The Structure of the First Coordination Shell in Liquid Water,” *Science* **304**, 995–999 (2004).
- ⁴S. T. Roberts, K. Ramasesha, and A. Tokmakoff, “Structural rearrangements in water viewed through two-dimensional infrared spectroscopy,” *Acc. Chem. Res.* **42**, 1239–1249 (2009).
- ⁵T. Head-Gordon and M. E. Johnson, “Tetrahedral structure or chains for liquid water,” *Proc. Nat. Acad. Sci. USA* **103**, 7973–7977 (2006).
- ⁶T. Head-Gordon and F. Paesani, “Water is not a dynamic polydisperse branched polymer,” *Proc. Nat. Acad. Sci. USA* **116**, 13169–13170 (2019).
- ⁷S. Naserifar and W. A. Goddard, “Reply to Head-Gordon and Paesani: Liquid water, a branched polymer with ~ 100 -fs short-lived heterogeneous hydrogen bonds,” *Proc. Nat. Acad. Sci. USA* **116**, 20257–20258 (2019).
- ⁸D. Ojha, K. Karhan, and T. D. Kühne, “On the Hydrogen Bond Strength and Vibrational Spectroscopy of Liquid Water,” *Sci. Rep.* **8**, 16888 (2018).
- ⁹A. B. McCoy, T. L. Guasco, C. M. Leavitt, S. G. Olesen, and M. A. Johnson, “Vibrational manifestations of strong non-Condon effects in the $\text{H}_3\text{O}^+\cdot\text{X}_3$ ($\text{X} = \text{Ar}, \text{N}_2, \text{CH}_4, \text{H}_2\text{O}$) complexes: A possible explanation for the intensity in the “association band” in the vibrational spectrum of water,” *Phys. Chem. Chem. Phys.* **14**, 7205–7214 (2012).
- ¹⁰J. O. Richardson, C. Pérez, S. Lobsiger, A. A. Reid, B. Temelso, G. C. Shields, Z. Kisiel, D. J. Wales, B. H. Pate, and S. C. Althorpe, “Concerted hydrogen-bond breaking by quantum tunneling in the water hexamer prism,” *Science* **351**, 1310–1313 (2016).
- ¹¹A. Rognoni, R. Conte, and M. Ceotto, “How many water molecules are needed to solvate one?” *Chem. Sci.* **12**, 2060–2064 (2021).
- ¹²A. Rognoni, R. Conte, and M. Ceotto, “Caldeira-Leggett model vs ab initio potential: A vibrational spectroscopy test of water solvation,” *J. Chem. Phys.* **154**, 094106 (2021).

- ¹³Y. Tong, T. Kampfrath, and R. K. Campen, “Experimentally probing the libration of interfacial water: The rotational potential of water is stiffer at the air/water interface than in bulk liquid,” *Phys. Chem. Chem. Phys.* **18**, 18424–18430 (2016).
- ¹⁴W. Fang, J. Chen, P. Pedevilla, X.-Z. Li, J. O. Richardson, and A. Michaelides, “Origins of fast diffusion of water dimers on surfaces,” *Nat. Commun.* **11**, 1689 (2020).
- ¹⁵R. M. Altman and G. L. Richmond, “Twist and Stretch: Assignment and Surface Charge Sensitivity of a Water Combination Band and Its Implications for Vibrational Sum Frequency Spectra Interpretations,” *J. Phys. Chem. B* **125**, 6717–6726 (2021).
- ¹⁶E. W. Castner, Y. J. Chang, Y. C. Chu, and G. E. Walrafen, “The intermolecular dynamics of liquid water,” *J. Chem. Phys.* **102**, 653–659 (1995).
- ¹⁷M. Freda, A. Piluso, A. Santucci, and P. Sassi, “Transmittance Fourier Transform Infrared Spectra of Liquid Water in the Whole Mid-Infrared Region: Temperature Dependence and Structural Analysis,” *Appl. Spectrosc.* **59**, 1155–1159 (2005).
- ¹⁸M. Heyden, J. Sun, S. Funkner, G. Mathias, H. Forbert, M. Havenith, and D. Marx, “Dissecting the THz spectrum of liquid water from first principles via correlations in time and space,” *Proc. Nat. Acad. Sci. USA* **107**, 12068–12073 (2010).
- ¹⁹T. Hasegawa and Y. Tanimura, “A polarizable water model for intramolecular and intermolecular vibrational spectroscopies,” *J. Phys. Chem. B* **115**, 5545–5553 (2011).
- ²⁰A. B. McCoy, “The role of electrical anharmonicity in the association band in the water spectrum,” *J. Phys. Chem. B* **118**, 8286–8294 (2014).
- ²¹G. R. Medders and F. Paesani, “Infrared and Raman Spectroscopy of Liquid Water through “First-Principles” Many-Body Molecular Dynamics,” *J. Chem. Theory Comput.* **11**, 1145–1154 (2015).
- ²²H. Ito, T. Hasegawa, and Y. Tanimura, “Effects of Intermolecular Charge Transfer in Liquid Water on Raman Spectra,” *J. Phys. Chem. Lett.* **7**, 4147–4151 (2016).
- ²³P. K. Verma, A. Kundu, M. S. Poretz, C. Dhoonmoon, O. S. Chegwidden, C. H. Londergan, and M. Cho, “The Bend+Libration Combination Band Is an Intrinsic, Collective, and Strongly Solute-Dependent Reporter on the Hydrogen Bonding Network of Liquid Water,” *J. Phys. Chem. B* **122**, 2587–2599 (2018).
- ²⁴D. Sidler, M. Meuwly, and P. Hamm, “An efficient water force field calibrated against intermolecular THz and Raman spectra,” *J. Chem. Phys.* **148**, 244504 (2018).

- ²⁵R. L. Benson, G. Trenins, and S. C. Althorpe, “Which quantum statistics–classical dynamics method is best for water?” *Faraday Discuss.* **221**, 350–366 (2019).
- ²⁶T. Morawietz, O. Marsalek, S. R. Pattenaude, L. M. Streacker, D. Ben-Amotz, and T. E. Markland, “The Interplay of Structure and Dynamics in the Raman Spectrum of Liquid Water over the Full Frequency and Temperature Range,” *J. Phys. Chem. Lett.* **9**, 851–857 (2018).
- ²⁷S. R. Pattenaude, L. M. Streacker, and D. Ben-Amotz, “Temperature and polarization dependent Raman spectra of liquid H₂O and D₂O,” *J. Raman Spectrosc.* **49**, 1860–1866 (2018).
- ²⁸M. Paolantoni, N. F. Lago, M. Albertí, and A. Laganà, “Tetrahedral Ordering in Water: Raman Profiles and Their Temperature Dependence,” *J. Phys. Chem. A* **113**, 15100–15105 (2009).
- ²⁹P. Hamm and M. Zanni, *Concepts and Methods of 2D Infrared Spectroscopy* (Cambridge University Press, 2011).
- ³⁰T. L. C. Jansen, S. Saito, J. Jeon, and M. Cho, “Theory of coherent two-dimensional vibrational spectroscopy,” *J. Chem. Phys.* **150**, 100901 (2019).
- ³¹I. A. Finneran, R. Welsch, M. A. Allodi, T. F. Miller, and G. A. Blake, “Coherent two-dimensional terahertz-terahertz-Raman spectroscopy,” *Proc. Nat. Acad. Sci. USA* **113**, 6857–6861 (2016).
- ³²I. A. Finneran, R. Welsch, M. A. Allodi, T. F. Miller, and G. A. Blake, “2D THz-THz-Raman Photon-Echo Spectroscopy of Molecular Vibrations in Liquid Bromoform,” *J. Phys. Chem. Lett.* **8**, 4640–4644 (2017).
- ³³I. B. Magdău, G. J. Mead, G. A. Blake, and T. F. Miller, “Interpretation of the THz-THz-Raman Spectrum of Bromoform,” *J. Phys. Chem. A* **123**, 7278–7287 (2019).
- ³⁴G. Mead, H. W. Lin, I. B. Magdău, T. F. Miller, and G. A. Blake, “Sum-Frequency Signals in 2D-Terahertz-Terahertz-Raman Spectroscopy,” *J. Phys. Chem. B* **124**, 8904–8908 (2020).
- ³⁵P. Hamm and J. Savolainen, “Two-dimensional-Raman-terahertz spectroscopy of water: Theory,” *J. Chem. Phys.* **136**, 094516 (2012).
- ³⁶J. Savolainen, S. Ahmed, and P. Hamm, “Two-dimensional Raman-terahertz spectroscopy of water,” *Proc. Nat. Acad. Sci. USA* **110**, 20402–20407 (2013).

- ³⁷P. Hamm, “2D-Raman-THz spectroscopy: A sensitive test of polarizable water models,” *J. Chem. Phys.* **141**, 184201 (2014).
- ³⁸P. Hamm and A. Shalit, “Perspective: Echoes in 2D-Raman-THz spectroscopy,” *J. Chem. Phys.* **146**, 130901 (2017).
- ³⁹M. Grechko, T. Hasegawa, F. D’Angelo, H. Ito, D. Turchinovich, Y. Nagata, and M. Bonn, “Coupling between intra-and intermolecular motions in liquid water revealed by two-dimensional terahertz-infrared-visible spectroscopy,” *Nat. Commun.* **9**, 885 (2018).
- ⁴⁰L. Vietze, E. H. G. Backus, M. Bonn, and M. Grechko, “Distinguishing different excitation pathways in two-dimensional terahertz-infrared-visible spectroscopy,” *J. Chem. Phys.* **154**, 174201 (2021).
- ⁴¹F. Novelli, B. Guchhait, and M. Havenith, “Towards Intense THz Spectroscopy on Water: Characterization of Optical Rectification by GaP, OH1, and DSTMS at OPA Wavelengths,” *Materials* **13**, 1311 (2020).
- ⁴²W. Zhao and J. C. Wright, “Doubly Vibrationally Enhanced Four Wave Mixing: The Optical Analog to 2D NMR,” *Phys. Rev. Lett.* **84**, 1411–1414 (2000).
- ⁴³M. Cho, “Theoretical description of two-dimensional vibrational spectroscopy by infrared-infrared-visible sum frequency generation,” *Phys. Rev. A* **61**, 023406 (2000).
- ⁴⁴H. Ito and Y. Tanimura, “Simulating two-dimensional infrared-Raman and Raman spectroscopies for intermolecular and intramolecular modes of liquid water,” *J. Chem. Phys.* **144**, 074201 (2016).
- ⁴⁵H.-W. Lin, G. Mead, and G. A. Blake, “Mapping LiNbO₃ Phonon-Polariton Nonlinearities with 2D THz-THz-Raman Spectroscopy,” *Phys. Rev. Lett.* (2022), Accepted Manuscript.
- ⁴⁶A. Shalit, S. Ahmed, J. Savolainen, and P. Hamm, “Terahertz echoes reveal the inhomogeneity of aqueous salt solutions,” *Nat. Chem.* **9**, 273–278 (2017).
- ⁴⁷A. Berger, G. Ciardi, D. Sidler, P. Hamm, and A. Shalit, “Impact of nuclear quantum effects on the structural inhomogeneity of liquid water,” *Proc. Nat. Acad. Sci. USA* **116**, 2458–2463 (2019).
- ⁴⁸G. Ciardi, A. Berger, P. Hamm, and A. Shalit, “Signatures of Intra- And Intermolecular Vibrational Coupling in Halogenated Liquids Revealed by Two-Dimensional Raman-Terahertz Spectroscopy,” *J. Phys. Chem. Lett.* **10**, 4463–4468 (2019).
- ⁴⁹S. J. Mousavi, A. Berger, P. Hamm, and A. Shalit, “Low-frequency anharmonic couplings in bromoform revealed from 2D Raman-THz spectroscopy: From the liquid to the crystalline

- phase,” J. Chem. Phys. **156**, 174501 (2022).
- ⁵⁰T. Hasegawa and Y. Tanimura, “Calculating fifth-order Raman signals for various molecular liquids by equilibrium and nonequilibrium hybrid molecular dynamics simulation algorithms,” J. Chem. Phys. **125**, 074512 (2006).
- ⁵¹H. Ito, T. Hasegawa, and Y. Tanimura, “Calculating two-dimensional THz-Raman-THz and Raman-THz-THz signals for various molecular liquids: The samplers,” J. Chem. Phys. **141**, 124503 (2014).
- ⁵²H. Ito, J.-Y. Jo, and Y. Tanimura, “Notes on simulating two-dimensional Raman and terahertz-Raman signals with a full molecular dynamics simulation approach,” Struct. Dyn. **2**, 054102 (2015).
- ⁵³X. Sun, “Hybrid equilibrium-nonequilibrium molecular dynamics approach for two-dimensional solute-pump/solvent-probe spectroscopy,” J. Chem. Phys. **151**, 194507 (2019).
- ⁵⁴J. E. Bertie and Z. Lan, “Infrared Intensities of Liquids XX: The Intensity of the OH Stretching Band of Liquid Water Revisited, and the Best Current Values of the Optical Constants of H₂O(l) at 25 °C between 15,000 and 1 cm⁻¹,” Appl. Spectrosc. **50**, 1047–1057 (1996).
- ⁵⁵S. Habershon, T. E. Markland, and D. E. Manolopoulos, “Competing quantum effects in the dynamics of a flexible water model,” J. Chem. Phys. **131**, 024501 (2009).
- ⁵⁶G. Avila, “Ab initio dipole polarizability surfaces of water molecule: Static and dynamic at 514.5nm,” J. Chem. Phys. **122**, 144310 (2005).
- ⁵⁷K. Töpfer, M. Upadhyay, and M. Meuwly, “Quantitative molecular simulations,” Phys. Chem. Chem. Phys. **24**, 12767–12786 (2022).
- ⁵⁸K. A. Jung, P. E. Videla, and V. S. Batista, “Inclusion of nuclear quantum effects for simulations of nonlinear spectroscopy,” J. Chem. Phys. **148**, 244105 (2018).
- ⁵⁹K. A. Jung, P. E. Videla, and V. S. Batista, “Multi-time formulation of Matsubara dynamics,” J. Chem. Phys. **151**, 034108 (2019).
- ⁶⁰K. A. Jung, P. E. Videla, and V. S. Batista, “Ring-polymer, centroid, and mean-field approximations to multi-time Matsubara dynamics,” J. Chem. Phys. **153**, 124112 (2020).
- ⁶¹T. Begušić, X. Tao, G. A. Blake, and T. F. Miller, “Equilibrium–nonequilibrium ring-polymer molecular dynamics for nonlinear spectroscopy,” J. Chem. Phys. **156**, 131102 (2022).

- ⁶²I. R. Craig and D. E. Manolopoulos, “Quantum statistics and classical mechanics: Real time correlation functions from ring polymer molecular dynamics,” *J. Chem. Phys.* **121**, 3368–3373 (2004).
- ⁶³M. Rossi, M. Ceriotti, and D. E. Manolopoulos, “How to remove the spurious resonances from ring polymer molecular dynamics,” *J. Chem. Phys.* **140**, 234116 (2014).
- ⁶⁴M. Rossi, V. Kapil, and M. Ceriotti, “Fine tuning classical and quantum molecular dynamics using a generalized Langevin equation,” *J. Chem. Phys.* **148**, 102301 (2018).
- ⁶⁵T. Seki, K.-Y. Chiang, C.-C. Yu, X. Yu, M. Okuno, J. Hunger, Y. Nagata, and M. Bonn, “The Bending Mode of Water: A Powerful Probe for Hydrogen Bond Structure of Aqueous Systems,” *J. Phys. Chem. Lett.* **11**, 8459–8469 (2020).
- ⁶⁶G. E. Walrafen and E. Pugh, “Raman combinations and stretching overtones from water, heavy water, and NaCl in water at shifts to ca. 7000 cm^{-1} ,” *J. Solution Chem.* **33**, 81–97 (2004).
- ⁶⁷J. R. Errington and P. G. Debenedetti, “Relationship between structural order and the anomalies of liquid water,” *Nature* **409**, 318–321 (2001).
- ⁶⁸P. Kumar, S. V. Buldyrev, and H. E. Stanley, “A tetrahedral entropy for water,” *Proc. Nat. Acad. Sci. USA* **106**, 22130–22134 (2009).
- ⁶⁹E. Duboué-Dijon and D. Laage, “Characterization of the Local Structure in Liquid Water by Various Order Parameters,” *J. Phys. Chem. B* **119**, 8406–8418 (2015).
- ⁷⁰M. Ceriotti, M. Parrinello, T. E. Markland, and D. E. Manolopoulos, “Efficient stochastic thermostating of path integral molecular dynamics,” *J. Chem. Phys.* **133**, 124104 (2010).